Indian J Phys (December 2025) 99(14):5645–5658
https://doi.org/10.1007/s12648-025-03750-6

ORIGINAL PAPER

Unveiling soliton dynamics in the unstable nonlinear schrödinger equation through computational and analytical exploration

A Farooq[1]*, W X Ma[1,4,5,6], S Rehman[2], J R M Borhan[3] and M M Miah[2,7]

[1]Department of Mathematics, Zhejiang Normal University, Zhejiang 321004, People's Republic of China

[2]Division of Mathematical and Physical Sciences, Kanazawa University, Kanazawa 920-1192, Japan

[3]Department of Mathematics, Jashore University of Science and Technology, Jashore 7408, Bangladesh

[4]Department of Mathematics, King Abdulaziz University, 21589 Jeddah, Saudi Arabia

[5]Department of Mathematics and Statistics, University of South Florida, Tampa 33620-5700, USA

[6]Material Science Innovation and Modelling, North-West University, Mmabatho 2735, South Africa

[7]Department of Mathematics, Khulna University of Engineering and Technology, Khulna 9203, Bangladesh

Received: 14 March 2025 / Accepted: 01 August 2025 / Published online: 8 October 2025

Abstract: This work examines the unstable nonlinear Schrödinger equation, which characterizes the temporal evolution of disturbances in marginally stable or unstable media. The $(\frac{G'}{G}, \frac{1}{G})$-expansion method is employed to derive new exact soliton solutions, explicitly represented through exponential, trigonometric, and rational functions. These exact solutions are then compared with results obtained from the Levenberg–Marquardt artificial neural network and the split-step Fourier numerical method. Statistical analyses, presented through tables and graphs, show strong agreement between the exact solutions and those obtained using these methods. Furthermore, 2-D, contour, and 3-D plots are utilized to visually represent and validate the behavior of the solutions. The results demonstrate that the combination of the $(\frac{G'}{G}, \frac{1}{G})$-expansion method, the Levenberg–Marquardt artificial neural network, and the split-step Fourier numerical method provides a robust and complementary framework for solving and analyzing the unstable nonlinear Schrödinger equation, offering reliable insights into its dynamic behavior.

Keywords: Unstable nonlinear Schrödinger's equation; Soliton solutions; $(\frac{G'}{G}, \frac{1}{G})$-expansion method; Levenberg-Marquardt algorithm; Split-step Fourier numerical method.

1. Introduction

Nonlinear ordinary and partial differential equations encompass a range of important problems across disciplines such as physics, chemistry, engineering, biology, and finance. Notable examples include environmental modeling, aircraft design, genetic motion, drug development, deep learning neural networks, and mean-field games in financial modeling. Nonlinear partial differential equations provide a fundamental mathematical framework for analyzing the behavior of complex physical phenomena characterized by nonlinear properties. They enable researchers to investigate intricate systems that would be difficult to understand otherwise. One significant area of focus is the investigation of optical solitons in nonlinear media [1]. Optical solitons, which are stable wave packets, play a crucial role in enabling high-speed data transfer in optical fibers and all-optical switches. Modern telecommunication systems benefit from their remarkable ability to maintain shape and intensity over long distances. This field of study aims to enhance our understanding of soliton dynamics and its applications, ultimately contributing to advancements in communication technology.

The utilization of various methodologies for finding exact solutions to nonlinear evolution equations and partial differential equations has demonstrated significant benefits

*Corresponding author, E-mail: aamirf@zjnu.edu.cn

and effectiveness. For a deeper understanding of nonlinear phenomena and realistic challenges, it is essential to discover closed-form soliton solutions of nonlinear partial differential equations. The study of such solutions has attracted considerable attention from contemporary mathematicians and physicists. In recent years, significant progress in nonlinear science has led to the development of numerous efficient methods for obtaining closed-form solutions to nonlinear partial differential equations. Some of the most widely used techniques include the $(\frac{G'}{G},\frac{1}{G})$-expansion method [2], the F-expansion method [3], the tanh–coth scheme [4], the Bessel collocation method [5], the trial solution method [6], the Tau method [7], the Hirota method [8], the simple equation method [9], the modified auxiliary equation method [10], the Riccati transformation approach [11], the Bernoulli sub-equation method [12], the Haar functions method [13], the Lie symmetry analysis [14], the Sardar sub-equation technique [15], the generalized $(\frac{G'}{G},\frac{1}{G})$-expansion method [16], the Painlevé analysis method [17, 18], the $(\frac{G'}{G'+G+A})$-expansion method [19], the reductive perturbation method [20], the variational iteration method [21], the r+mEDAM method [22], the sub-equation method [23], the advanced algebraic method [24], the modified Exp-function method [25], the modified $(\frac{G'}{G^2})$-expansion method [26], among others.

One of the most recently developed methods in this area is the $(\frac{G'}{G},\frac{1}{G})$-expansion technique. This innovative approach enables the efficient and straightforward solution of many nonlinear partial differential equations and is regarded as one of the most modern and comprehensive methods in the field. Despite its potential, the method has seen relatively limited application in recent years; however, several notable findings have emerged. Initially, Li et al. [27] introduced a novel extension known as the two-variable $(\frac{G'}{G},\frac{1}{G})$-expansion method, which produced numerous new traveling wave solutions for the Zakharov equations, solutions that have proven valuable for analytical studies. Various characteristics of the system have been examined in these investigations, supporting a wide range of applications. In our recent work, we derived rational, complex trigonometric, hyperbolic, and trigonometric traveling wave solutions to the Jimbo–Miwa equation in three spatial dimensions and one additional dimension using the $(\frac{G'}{G},\frac{1}{G})$-expansion method. Moreover, recent studies such as [28] have employed similar approaches to obtain closed-form soliton solutions of nonlinear differential equations.

In the 1990 s, artificial neural networks (ANNs) were applied to solve ordinary and partial differential equations [29]. However, due to technological limitations at the time, this line of research did not attract widespread attention. The recent explosion of data and advances in computational power have driven remarkable progress in machine learning, especially in deep learning, leading to breakthroughs in areas such as image recognition [30], natural language processing [31], and equation solving [32]. Machine learning has demonstrated substantial potential in diverse applications, including simulation, predictive modeling, and the representation of physical processes across multiple scales [33]. A major advancement in this context was the introduction of physics-informed neural networks (PINNs) by Raissi et al. [34]. These networks are specifically designed to solve supervised learning problems while respecting physical laws formulated through general nonlinear partial differential equations. Their framework addressed two primary challenges: (1) data-driven solutions of PDEs and (2) data-driven discovery of governing PDEs. They proposed two algorithmic strategies, continuous-time and discrete-time models, depending on the nature and structure of the available data. Among the various training algorithms for ANNs, the Levenberg–Marquardt and Newton methods stand out due to their use of second-order partial derivatives of the cost function to optimize weights during training and testing. These algorithms have demonstrated novel applicability in numerous studies and are considered promising alternatives for ANN training. For example, in [35], the authors employed intelligent computing techniques alongside Levenberg–Marquardt ANNs to model the nonlinear dynamics of COVID-19 epidemics, with the aim of supporting future disease management. In another study [36], the Levenberg–Marquardt ANN successfully recovered peakon and solitary wave solutions of the Lax equation.

There is no study in the existing literature that combines the $(\frac{G'}{G},\frac{1}{G})$-expansion approach with the Levenberg–Marquardt artificial neural network and the split-step Fourier numerical method to solve the unstable nonlinear Schrödinger equation. Motivated by this gap, we are the first to address this challenge by integrating these methods to provide a robust and flexible framework for solving such nonlinear partial differential equations. The $(\frac{G'}{G},\frac{1}{G})$-expansion approach efficiently derives exact soliton solutions with explicit analytical expressions, but its complexity increases with more intricate models. The Levenberg–Marquardt artificial neural network and the split-step Fourier numerical methods are used to validate solutions, check convergence, and reduce errors, especially when analytical methods have limitations. This integrated approach improves precision and adaptability, outperforming traditional methods like the Hirota bilinear method [37] or inverse scattering transform [38], which are often limited to specific cases. The proposed methodology is applied to derive new exact solutions for the unstable nonlinear Schrödinger equation, which are further refined and validated using the Levenberg–Marquardt artificial neural network and the split-step Fourier numerical method [39].

The remainder of the manuscript is organized as follows. Section 2 presents the complete methodology of the $(\frac{G'}{G}, \frac{1}{G})$-expansion approach and the Levenberg–Marquardt artificial neural network. In Sect. 3, explicit expressions for the exact solutions of the unstable nonlinear Schrödinger equation are derived using the $(\frac{G'}{G}, \frac{1}{G})$-expansion method, followed by the application of the Levenberg–Marquardt artificial neural network and the split-step Fourier numerical method. Section 4 provides a graphical representation of the solutions obtained using the $(\frac{G'}{G}, \frac{1}{G})$-expansion method, the Levenberg–Marquardt artificial neural network, and the split-step Fourier numerical method. Finally, Sect. 5 concludes the paper.

2. Formulation for the $(\frac{G'}{G}, \frac{1}{G})$-expansion approach and the Levenberg-Marquardt artificial neural network

To begin, we present the complete procedure for solving the unstable nonlinear Schrödinger equation using the $(\frac{G'}{G}, \frac{1}{G})$-expansion approach. Additionally, we provide a concise overview of how the Levenberg–Marquardt artificial neural network algorithm can be applied to examine the solutions produced by the $(\frac{G'}{G}, \frac{1}{G})$-expansion technique.

2.1. Methodology of the $(\frac{G'}{G}, \frac{1}{G})$-expansion method

In this section, we examine the primary formulation procedures of the two-variable $(\frac{G'}{G}, \frac{1}{G})$-expansion method to derive novel optical soliton solutions for the unstable nonlinear Schrödinger equation. The auxiliary linear ODE is defined as follows:

$$\frac{d^2G}{d\kappa^2} + \lambda G = v, \tag{1}$$

where λ and v are the constant parameters, and the following expression represents two parameters:

$$\vartheta = \frac{G'(\kappa)}{G(\kappa)}, \Omega = \frac{1}{G(\kappa)}. \tag{2}$$

Thus, we obtained

$$\vartheta' = -\vartheta^2 + v\Omega - \lambda, \Omega' = -\vartheta\Omega. \tag{3}$$

The solution to (1) varies with (1) depending on λ and is categorized into three scenarios:

Case a For $\lambda < 0$, the typical solution to (1) is,

$$G = S_1 \sinh(\sqrt{-\lambda}\kappa) + S_2 \cosh(\sqrt{-\lambda}\kappa) + \frac{v}{\lambda}, \tag{4}$$

where S_1 and S_2 represent two arbitrary constants. Following this, we obtain

$$\Omega^2 = \frac{-\lambda(\vartheta^2 - 2v\Omega + \lambda)}{\lambda^2\omega_1 + v^2} \quad \text{and} \quad \omega_1 = S_1^2 - S_2^2. \tag{5}$$

Case b For $\lambda > 0$, the typical solution to (1) is,

$$G = S_1 \sin(\sqrt{\lambda}\kappa) + S_2 \cos(\sqrt{\lambda}\kappa) + \frac{v}{\lambda}, \tag{6}$$

hence, we have

$$\Omega^2 = \frac{\lambda(\vartheta^2 - 2v\Omega + \lambda)}{\lambda^2\omega_2 - v^2} \quad \text{and} \quad \omega_2 = S_1^2 + S_2^2. \tag{7}$$

Case c. For $\lambda = 0$, the typical solution to (1) is,

$$G = \frac{v}{2}\kappa^2 + S_1\kappa + S_2, \tag{8}$$

Thus, we have

$$\Omega^2 = \frac{(\vartheta^2 - 2v\Omega)}{S_1^2 - 2v^2 S_2}. \tag{9}$$

Take the non-linear evolution equation in four independent constraints x, y, z and t in the below polynomial

$$K(u, u_t, u_x, u_y, u_z, u_{tt}, u_{xx}, u_{yy}, u_{zz}, u_{xy}, u_{xt}, \ldots) = 0, \tag{10}$$

Here, we utilized the subscripts to describe the partial derivatives (for instance: $u_t = \frac{\partial u}{\partial t}, u_{tt} = \frac{\partial^2 u}{\partial t^2}$, etc.) and substituted a new wave parameter κ that coincided with the independent constraints as follows:

$$u(x, y, z, t) = u(\kappa), \kappa = x + y + z - at. \tag{11}$$

Considering (11) into (10), an ODE for $u(\kappa)$ transfer as,

$$Q(u, -au', u', u', u', a^2u'', u'', u'', u'', \ldots) = 0. \tag{12}$$

where, a denotes the velocity of wave and Q stands for the polynomial of $u(\kappa)$ and its corresponding derivatives. Suppose that, by the help of two constraints, $(\frac{G'}{G}, \frac{1}{G})$-expansion method, the solution of the ODE (12) has the following form:

$$u(\kappa) = \sum_{i=0}^{J} d_i \phi^i(\kappa) + \sum_{i=1}^{J} e_i \phi^{i-1}(\kappa)\xi(\kappa). \tag{13}$$

In this expression, d_i, e_i are constants, while the positive integer J is defined as the homogeneous balance number. We determined the arbitrary constants by applying the two constraints of the $(\frac{G'}{G}, \frac{1}{G})$-expansion method. Additional procedural details are in the reference [27].

2.2. Methodology of the Levenberg-Marquardt artificial neural network algorithm

This subsection employs MATLAB's Neural Fitting Tool (nftool) to explore an effective setup for solving an input–output fitting problem using an artificial neural network (ANN), where the target output is derived from the solution obtained via the $(\frac{G'}{G}, \frac{1}{G})$-expansion method. The tool provides a user-friendly interface for importing data, configuring the network architecture, training, and evaluating performance. To ensure adaptability to the specific characteristics of our dataset and to enhance fitting accuracy, we further developed a custom algorithm using MATLAB's scripting environment. Although MATLAB was used for implementation, the core training process is based on the Levenberg–Marquardt backpropagation algorithm. For the complete mathematical steps and theoretical formulation of the LM-ANN approach, please refer to [40].

We outlined two cases for deploying the Levenberg–Marquardt artificial neural network. In the first case, the variable x was varied while keeping t constant in the solutions obtained from the $(\frac{G'}{G}, \frac{1}{G})$-expansion method. In the second case, we manipulated the value of t while keeping x constant for the same set of equations. To implement the data division strategy, we allocated 70% of the dataset for training, 15% for validation, and 15% for testing. This partitioning was carried out using MATLAB's dividerand function, which randomly separates the data according to the specified ratios. Such a partitioning strategy is essential, as it enables the model to learn from a substantial portion of the data (training set), tune its parameters using a smaller subset (validation set), and evaluate its performance on unseen data (testing set). The Levenberg–Marquardt backpropagation method (trainlm) was selected for training due to its effectiveness and efficiency in networks of medium size. This approach is particularly advantageous when fast training is required and memory resources are not severely limited. The network architecture was defined with a single hidden layer containing ten neurons. This configuration was chosen to minimize the risk of overfitting while maintaining sufficient complexity to capture the underlying patterns in the data. To improve convergence during training, constant rows were removed to eliminate duplicate data, and mapminmax was used to normalize the input and output values.

3. Application of analytical and Levenberg-Marquardt artificial neural network algorithm

In this section, we apply the $(\frac{G'}{G}, \frac{1}{G})$-expansion method and the Levenberg-Marquardt artificial neural network algorithm to solve the unstable nonlinear Schrödinger equation.

3.1. Unstable non-linear Schrödinger equation

In this sub-section, we analyze the optical soliton solutions of the unstable nonlinear Schrödinger equation, which is widely used to model the propagation and evolution of deep-sea internal waves due to its detailed representation of ocean dispersion and nonlinearity [41]. The unstable nonlinear Schrödinger equation, a variation of the nonlinear Schrödinger equation where the roles of space and time are reversed, plays a key role in plasma dynamics and describes two-layer baroclinic instabilities [42]. In [42], it was shown that equilibrated finite-amplitude states induce oscillations in both mean flow and baroclinic waves in the absence of dissipation. Additionally, [43] proposed a nonlinear theory for acoustic wave propagation in piezoelectric semiconductors using asymptotic expansions. Several researchers, including Lu et al. [44], have developed dark and bright solitons, solitary waves, and periodic solutions for the unstable nonlinear Schrödinger equation, which describe the temporal evolution of disturbances in moderately stable or unstable media. Recently, more closed-form solutions have been proposed [45], further advancing the understanding of this equation. The unstable nonlinear Schrödinger equation [43] is represented in the following form:

$$i\frac{\partial\Theta}{\partial t} + \frac{\partial^2\Theta}{\partial x^2} + 2\varphi|\Theta(x,t)|^2\Theta(x,t) - 2\beta\Theta = 0, \tag{14}$$

where the wave outline function is denoted by $\Theta(x,t)$, $i = \sqrt{-1}$, φ and β are arbitrary constants. To obtain the new closed-form traveling wave solutions of the system in (14), we must convert (14) into a nonlinear ODE using the complex transformation outlined below:

$$\Theta(x,t) = T(\kappa)\exp(i\theta(x,t)), \tag{15}$$

where, $\kappa = x + at$, and x is stands for space variable, a portrays velocity of wave and t demonstrates time variable. For $\theta(x,t) = \gamma x + \chi t$, $\theta(x,t)$ represents phase component, γ

is the wave number and χ is the frequency. After introducing (15)) into (14), one can obtain the complex Eq. and then separate the real and imaginary parts. So, the real parts are as follows:

$$T'' - (\gamma^2 + \chi + 2\beta)T + 2\varphi T^3 = 0, \tag{16}$$

here, the coefficient of the imaginary term is $a = -2\gamma$. To acquire the estimation of a positive integer J, utilize the homogeneous balance principle, i.e., by balancing the highest-order derivative and the nonlinear terms in (16). So, $J + 2 = 3J \Rightarrow J = 1$. By our declaration, let us consider the solution of (16) as follows:

$$T(\kappa) = d_0 + d_1\vartheta(\kappa) + e_1\Omega(\kappa), \tag{17}$$

where d_0, d_1 and e_1 are constants to consider, and we explore three types:

Type 1 For hyperbolic function ($\lambda < 0$)

Inserting (17) with (3) and (5) into (16), by equating all the coefficients of the polynomial in ϑ and Ω, to zero, we obtain a system of algebraic equations. Upon solving these equations using Mathematica software, we determine the following estimates for the constants:

$$d_0 = 0, d_1 = \pm\frac{1}{2\sqrt{-\varphi}}, e_1 = \pm\frac{\sqrt{(\omega_1\lambda^2 + v^2)}}{2\sqrt{\varphi\lambda}},$$
$$\chi = \frac{-2\gamma^2 - 4\beta + \lambda)}{2},$$

when introducing the above values in (17), then we acquired

$$T(\kappa) = \pm\frac{1}{2\sqrt{-\varphi}}\vartheta(\kappa) \pm \frac{\sqrt{(\omega_1\lambda^2 + v^2)}}{2\sqrt{\varphi\lambda}}\Omega(\kappa), \tag{18}$$

Utilizing (2) and (4)), then we have

$$T(\kappa) = \pm\frac{\sqrt{\lambda}(S_1\cosh(\sqrt{-\lambda}\kappa) + S_2\sinh(\sqrt{-\lambda}\kappa))}{2\sqrt{\varphi}(S_1\sinh(\sqrt{-\lambda}\kappa) + S_2\cosh(\sqrt{-\lambda}\kappa) + \frac{v}{\lambda})} \pm \frac{\sqrt{\omega_1\lambda^2 + v^2}}{2\sqrt{\varphi\lambda}(S_1\sinh(\sqrt{-\lambda}\kappa) + S_2\cosh(\sqrt{-\lambda}\kappa) + \frac{v}{\lambda})}, \tag{19}$$

then the closed-form solution of (14) as follows

$$\Theta(x,t) = \Big(\pm\frac{\sqrt{\lambda}(S_1\cosh(\sqrt{-\lambda}(x-2\gamma t) + S_2\sinh(\sqrt{-\lambda}(x-2\gamma t)))}{2\sqrt{\varphi}(S_1\sinh(\sqrt{-\lambda}(x-2\gamma t)) + S_2\cosh(\sqrt{-\lambda}(x-2\gamma t)) + \frac{v}{\lambda})} \pm \frac{\sqrt{\omega_1\lambda^2 + v^2}}{2\sqrt{\varphi\lambda}(S_1\sinh(\sqrt{-\lambda}(x-2\gamma t)) + S_2\cosh(\sqrt{-\lambda}(x-2\gamma t)) + \frac{v}{\lambda})}\Big)\exp(i(\gamma x + \chi t)), \tag{20}$$

As a special case, we consider $S_2 = 0, S_1 \neq 0$ and $v = 0$, then we obtain

$$\Theta(x,t) = \Big(\pm\frac{\sqrt{\lambda}(\coth(\sqrt{-\lambda}(x-2\gamma t)}{2\sqrt{\varphi}} \pm \frac{\sqrt{\lambda}\ (csch(\sqrt{-\lambda}(x-2\gamma t))}{2\sqrt{\varphi}}\Big)\exp(\imath(\gamma x + \chi t)) \tag{21}$$

Here, $\varphi < 0$, and $\chi = \frac{2\gamma^2 + 4\beta - \lambda)}{2}$.

Type 2 For trigonometric function ($\lambda > 0$)

Introducing (17)) along with (3) and (7) into (16) and setting the entire coefficients of ϑ and Ω equal to zero and solving the system of equations, we acquire the following unknown constants,

$$d_0 = 0, d_1 = \pm\frac{1}{2\sqrt{-\varphi}}, e_1 = \pm\frac{\sqrt{(\omega_2\lambda^2 - v^2)}}{2\sqrt{-\varphi\lambda}},$$
$$\chi = \frac{-2\gamma^2 - 4\beta + \lambda)}{2},$$

Substituting the above estimations in (17), we have

$$T(\kappa) = \pm\frac{1}{2\sqrt{-\varphi}}\vartheta(\kappa) \pm \frac{\sqrt{(\omega_2\lambda^2 - v^2)}}{2\sqrt{-\varphi\lambda}}\Omega(\kappa), \tag{22}$$

Using (2) and (6) in (22), then we achieved

$$T(\kappa) = \pm \frac{\sqrt{\lambda}(S_1 \cos(\sqrt{\lambda}\kappa) - S_2 \sin(\sqrt{\lambda}\kappa))}{2\sqrt{-\varphi}(S_1 \sin(\sqrt{\lambda}\kappa) + S_2 \cos(\sqrt{\lambda}\kappa) + \frac{v}{\lambda})} \pm \frac{\sqrt{(\omega_2\lambda^2 - v^2)}}{2\sqrt{-\varphi\lambda}(S_1 \sin(\sqrt{\lambda}\kappa) + S_2 \cos(\sqrt{\lambda}\kappa) + \frac{v}{\lambda})}, \tag{23}$$

Then the exact soliton solution of (14) is given as

$$\Theta(x,t) = \Big(\pm \frac{\sqrt{\lambda}(S_1 \cos(\sqrt{\lambda}(x-2\gamma t)) - S_2 \sin(\sqrt{\lambda}(x-2\gamma t)))}{2\sqrt{-\varphi}(S_1 \sin(\sqrt{\lambda}(x-2\gamma t)) + S_2 \cos(\sqrt{\lambda}(x-2\gamma t)) + \frac{v}{\lambda})} \pm \frac{\sqrt{(\omega_2\lambda^2 - v^2)}}{2\sqrt{-\varphi\lambda}(S_1 \sin(\sqrt{\lambda}(x-2\gamma t)) + S_2 \cos(\sqrt{\lambda}(x-2\gamma t)) + \frac{v}{\lambda})} \Big) \exp(i(\gamma x + \chi t)), \tag{24}$$

For special case, we take $S_1 \neq 0, S_2 = 0$ and $v = 0$, so we have

$$\Theta(x,t) = \Big(\pm \frac{\sqrt{\lambda}(\cot(\sqrt{\lambda}(x-2\gamma t)))}{2\sqrt{-\varphi}} \pm \frac{\sqrt{\lambda}(\csc(\sqrt{\lambda}(x-2\gamma t)))}{2\sqrt{-\varphi}} \Big) \exp(i(\gamma x + \chi t)), \tag{25}$$

For $\varphi < 0$ and $\chi = \frac{-2\gamma^2 - 4\beta + \lambda)}{2}$.

Type 3 Rational function ($\lambda = 0$)

Similarly, put (17)) with (3) and (8)) into (16), for all the coefficients of ϑ and Ω is equal to zero, then we have the constant like below

$$d_0 = 0, d_1 = \pm \frac{1}{2\sqrt{-\varphi}}, e_1 = \pm \frac{\sqrt{S_1^2 - 2vS_2}}{2\sqrt{-\varphi}}, \chi = -\gamma^2 - 2\beta,$$

The closed-form solution of (14), using the above constants and (3) and (8)), then we have

$$\Theta(x,t) = \Big(\pm \frac{(v(x-2\gamma t) + S_1)}{2\sqrt{-\varphi}(\frac{v}{2}(x-2\gamma t)^2 + S_1(x-2\gamma t) + S_2)} \pm \frac{\sqrt{(S_1^2 - 2S_2 v)}}{2\sqrt{-\varphi}(\frac{v}{2}(x-2\gamma t)^2 + S_1(x-2\gamma t) + S_2)} \Big) \exp(i(\gamma x + \chi t)). \tag{26}$$

where $\varphi < 0$ and $\chi = -\gamma^2 - 2\beta$.

3.2. Levenberg-Marquardt artificial neural network analysis for the (14)

This subsection demonstrates the application of the Levenberg-Marquardt artificial neural network algorithm to the soliton solutions derived from the (14). The Levenberg-Marquardt artificial neural network's performance is assessed by analyzing necessary statistical measures like regression curves, fitting, error curves, and mean square error analysis. These analyses validate the solutions' dependability and precision, showcasing the Levenberg-Marquardt artificial neural network's efficacy in representing the nonlinear dynamics of both equations.

The first three tables (1, 2, 3) evaluate the performance of Levenberg-Marquardt artificial neural network simulations for solving the (14) as outlined in (20), (24), and (26). In Table 1, Case I achieves efficient convergence with relatively low MSE across all phases, whereas Case II, despite more extended training, shows higher MSE and slightly lower performance. Table 2 highlights that Case I, though taking longer to compute, delivers moderate accuracy, while Case II offers improved accuracy and faster convergence, albeit with a lower performance metric. In Table 3, Case II outshines Case I with significantly lower MSE but at the cost of greater computational demands, striking a balance between precision and resource consumption.

3.3. Statistical analysis for the Levenberg-Marquardt algorithm and the numerical results

The performance of the results obtained by the Levenberg-Marquardt algorithm and the split-step Fourier numerical method [39] was assessed using various statistical measures for (20), (24), and (26). This array includes the Correlation Coefficient (R), the Coefficient of Determination (R^2), the Mean Absolute Error (MAE), the Mean Squared Error (MSE), the Root Mean Squared Error (RMSE), as well as the minimum (Min), maximum (Max), mean, standard deviation (SD), and median (MD). Additionally, it includes the mathematical formulations of statistical operators such as the Semi-Interquartile Range (SIR) and Theil's Inequality Coefficients (TIC). We provide further details on these metrics, as they are essential for examining the effectiveness of the methods.

Table 1 Approximation of (20) using Levenberg-Marquardt artificial neural network

Case	MSE			Performance	Grad	Mu	Epochs	Time
	Training	Testing	Validation					
I	2.40E−07	1.20E−05	6.40E−05	2.54E−07	8.70E−08	1.00E−09	205	0 m 50 s
II	6.60E−07	3.00E−05	1.70E−05	1.61E−08	9.94e−08	1.00E−08	701	1 m 47 s

Table 2 Approximation of (24) using Levenberg-Marquardt artificial neural network

Case	MSE			Performance	Grad	Mu	Epochs	Time
	Training	Testing	Validation					
I	1.00E−03	5.80E−03	4.00E−03	5.12E−06	3.09E−03	1.00E−08	445	1 m 10 s
II	1.90E−04	9.50E−05	3.10E−04	1.21E−05	1.67E−04	1.00E−08	38	0 m 7 s

Table 3 Approximation of (26) using Levenberg-Marquardt artificial neural network

Case	MSE			Performance	Grad	Mu	Epochs	Time
	Training	Testing	Validation					
I	4.80E-03	2.60E-02	6.70E-03	8.61E-05	5.97E-06	1.00E-09	238	1 m 0 s
II	6.70E-05	3.70E-03	3.30E-04	4.06E-06	9.00E-06	1.00E-07	274	1 m 17 s

Table 4 Statistical measures for exact, numerical, and predicted values by Levenberg-Marquardt artificial neural network of (20) for $t = 1$

Statistical measure	Exact values	Numerical values	Predicted values
Min	0.069339	0.069341	0.06979
SIR	0.0054804	0.0055914	0.0054044
MD	0.49997	0.49996	0.49993
SD	0.10384	0.10384	0.10384
Mean	0.49188	0.49188	0.49188
Max	0.71258	0.71258	0.7127
RMSE	–	0.00042404	0.00013302
MAE	–	2.7286e−05	8.489e−05
MAPE	–	0.0055657	0.00030393
MSE	–	1.7981e−07	1.7693e−08
R	–	0.99999	0.99999
R^2	–	0.99998	1
TIC	–	0.00042176	0.0001323

$$\mathrm{RMSE} = \sqrt{\frac{1}{n}\sum_{i=1}^{n}\left(Y_i^{\mathrm{exact}} - Y_i^{\mathrm{estimated}}\right)^2},$$

$$\mathrm{MAE} = \frac{1}{n}\sum_{i=1}^{n}\left|Y_i^{\mathrm{exact}} - Y_i^{\mathrm{estimated}}\right|,$$

$$\mathrm{MAPE} = \frac{1}{n}\sum_{i=1}^{n}\left|\frac{Y_i^{\mathrm{exact}} - Y_i^{\mathrm{estimated}}}{Y_i^{\mathrm{actual}}}\right|,$$

$$\mathrm{MSE} = \frac{1}{n}\sum_{i=1}^{n}\left(Y_i^{\mathrm{exact}} - Y_i^{\mathrm{estimated}}\right)^2,$$

$$R^2\text{-score} = 1 - \frac{\sum_{i=1}^{n}\left(Y_i^{\mathrm{exact}} - Y_i^{\mathrm{estimated}}\right)^2}{\sum_{i=1}^{n}\left(Y_i^{\mathrm{exact}} - \mu\right)^2},$$

$$R\text{-score} = \frac{\sum_{i=1}^{n}\left(Y_i^{\mathrm{exact}} - \bar{Y}\right)\left(Y_i^{\mathrm{exact}} - Y_i^{\mathrm{estimated}}\right)}{\sqrt{\sum_{i=1}^{n}\left(Y_i^{\mathrm{exact}} - \bar{Y}\right)^2}\sqrt{\sum_{i=1}^{n}\left(Y_i^{\mathrm{exact}} - Y_i^{\mathrm{estimated}}\right)^2}},$$

$$\mathrm{SIR} = -\frac{1}{2}\left(\text{Quartile } 1 - \text{Quartile } 3\right),$$

$$\mathrm{TIC} = \frac{\sqrt{\frac{1}{n}\sum_{i=1}^{n}\left(\left(Y_i^{\mathrm{exact}} - Y_i^{\mathrm{estimated}}\right)^2\right.}}{\sqrt{\frac{1}{n}\sum_{i=1}^{n}\left(Y_i^{\mathrm{exact}}\right)^2} + \sqrt{\frac{1}{n}\sum_{i=1}^{n}\left(Y_i^{\mathrm{estimated}}\right)^2}},$$

where n is the number of observations.

Table 5 Statistical measures for exact, numerical, and predicted values of by Levenberg-Marquardt artificial neural network of (24)

Statistical measure	Exact values	Numerical values	Predicted values
Min	0.005153	0.0033814	0.053515
SIR	0.062223	1.4683	1.4394
MD	1.4004	1.6193	1.4406
SD	4.2303	4.1997	4.2266
Mean	3.0725	3.1673	3.0719
Max	19.9833	19.9593	19.8616
RMSE	–	0.003788	0.0023134
MAE	–	0.00096414	0.0010472
MAPE	–	0.0085656	0.0075218
MSE	–	1.4349e−05	5.3519e−06
R	–	0.99918	1
R^2	–	1	0.99987
TIC	–	0.00036012	0.0011

Input:
Set parameters used in Eqs. (20), (24), (26).
Spatial values: $x = [-10, 10]$
Time values: $t = [0, 0.5, 1, 1.5, 2]$
Domain parameters: $L_x = 2000$, number of spatial points $N_x = 1000$, time step $\Delta t = 0.0001$
Output:
Numerical solution using the Split-Step Fourier Method
Statistical metrics for error analysis
Initialize arrays to store solutions and statistical metrics for error analysis.
for each time value t **do**
  Define the analytical solutions for Eq. (14).
  Evaluate the analytical solution for each x-value.
  Store the analytical solution for comparison.
end for
Initialize the numerical solution using the specified initial conditions for Eqs. (20), (24), and (26).
$k \leftarrow \frac{2\pi}{L_x} \times \mathrm{range}([0 : \frac{N_x}{2} - 1, -\frac{N_x}{2} : -1])$
$D \leftarrow \exp\left(-i \cdot (k^2 + 2 \cdot \beta) \cdot \Delta t / 2\right)$
$\Theta \leftarrow \mathrm{arrayfun}(\mathrm{initial\_solution}, x)$
for each n from 1 to N_t **do**
  $\Theta \leftarrow \Theta \cdot \exp\left(-i \cdot 2 \cdot \phi \cdot \mathrm{abs}(\Theta)^2 \cdot \Delta t\right)$
  $\Theta_{\mathrm{hat}} \leftarrow \mathrm{fft}(\Theta)$
  $\Theta_{\mathrm{hat}} \leftarrow D \cdot \Theta_{\mathrm{hat}}$
  $\Theta \leftarrow \mathrm{ifft}(\Theta_{\mathrm{hat}})$
end for
Compute error between analytical and numerical solutions at $t = 1$.
Plot both the analytical and numerical solutions for comparison.
Visualize the error between the two solutions.
Compute statistical metrics to assess the accuracy and effectiveness of the numerical method.

Algorithm 1 MATLAB Implementation for the Numerical Soliton Solutions of Eq. (14)

Table 6 Statistical measures for exact, numerical, and predicted values by Levenberg-Marquardt artificial neural network of (20)

Statistical measure	Exact values	Numerical values	Predicted values
Min	0.26726	0.26743	0.239794
SIR	0.14946	0.14946	0.14531
MD	0.45428	0.45428	0.45671
SD	0.19557	0.19557	0.19523
Mean	0.51479	0.51479	0.51479
Max	0.97349	0.97349	0.97434
RMSE	–	4.6078e−05	0.00013302
MAE	–	4.6697e−06	8.489e−05
MAPE	–	0.0011424	0.00030393
MSE	–	2.1232e−09	1.7693e−08
R	–	1	1
R^2	–	1	1
TIC	–	4.184e−05	0.0000323

The presented results in Tables 4, 5, and 6 provide a comprehensive comparison of the exact, numerical, and predicted values generated by the Levenberg-Marquardt artificial neural network for three distinct solutions of the (14). These tables utilize several key statistical measures to assess the accuracy and performance of the Levenberg-Marquardt artificial neural network in approximating the exact solutions, making it a crucial component for validating the neural network and numerical results.

In Table 4, corresponding to the solution of (14) by (20) at $t = 1$, various statistical measures, including Min, SIR, MID, SD, Mean, and Max, demonstrate that both the numerical and Levenberg-Marquardt artificial neural network-predicted values closely align with the exact values. The Levenberg-Marquardt artificial neural network achieves an exceptional regression coefficient $R = 0.99999$, $R^2 = 1$, indicating a near-perfect approximation. Moreover, error metrics such as RMSE, MAE, MAPE, MSE, and TIC are remarkably low, confirming that the neural network produces highly accurate predictions with minimal error.

Table 5, which relates to the solution of (14) by (24), further reinforces the effectiveness of the Levenberg-Marquardt artificial neural network. The statistical measures for this solution show minimal differences between exact, numerical, and predicted values for critical metrics such as SIR, SD, and Mean, reflecting the precision of the Levenberg-Marquardt artificial neural network in capturing the dynamics of the (20). The regression results from $R = 1$, $R^2 = 0.99987$ again demonstrate excellent performance, with low RMSE, MAE, MAPE, and MSE error values. Although minor deviations are present in the error measures, particularly with RMSE and MAE, the ANN exhibits robust predictive capabilities.

Finally, in Table 6, corresponding to another solution of the (14), the Levenberg-Marquardt artificial neural network accuracy is highlighted by the statistical measures, where Min, SIR, MD, SD, Mean, and Max from the predicted values match closely with the exact and numerical results. The regression metrics $R = 1$, $R^2 = 1$ confirm a perfect fit, and the error measures (RMSE, MAE, MAPE, MSE, TIC) are extremely low, reinforcing the model's precision in predicting the solution with negligible error.

Across all the Tables 4, 5, and 6, the Levenberg-Marquardt artificial neural network and the Split-Step Fourier numerical method consistently demonstrate high precision and reliability in approximating complex nonlinear (14). The consistently low error values and near-perfect regression results affirm the network's robustness and effectiveness in capturing the dynamics of the (14). These findings illustrate the strength of the Levenberg-Marquardt artificial neural network in solving soliton-based problems and validate its potential application for broader nonlinear wave dynamics, making this approach highly attractive to both researchers and reviewers in the field of computational mathematics and soliton theory.

4. Graphical discussion

In this section, we present a detailed graphical analysis to validate the theoretical results derived in previous sections. All computations were performed using MATLAB R2023a.

Figures 1, 2, 3, 4, 5, 6, 7, 8, 9 visualize soliton solutions of the (14). These include exact solutions from equations (20), (24), and (26), numerical solutions generated by Algorithm 1, and results from Levenberg-Marquardt

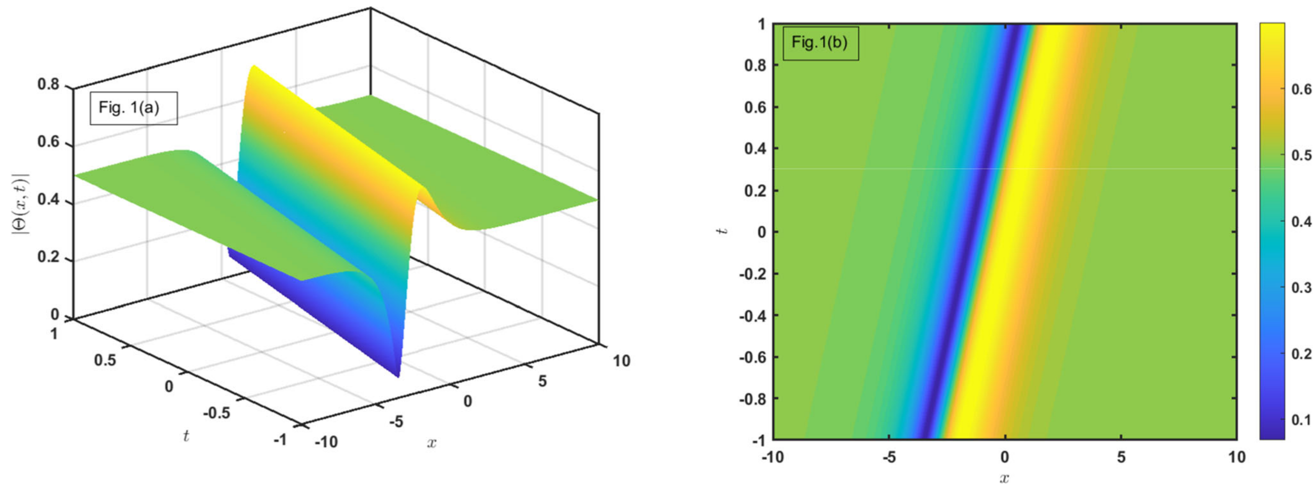

Fig. 1 Figures of (20) are provided for the constants as follows, $S_1 = 1,\ S_2 = 2,\ \lambda = -1,\ v = 1,\ \varphi = -1,\ \gamma = 1,\ \beta = 1,\ \omega_1 = 1$, and $t = 1.0$ (for $3D$)

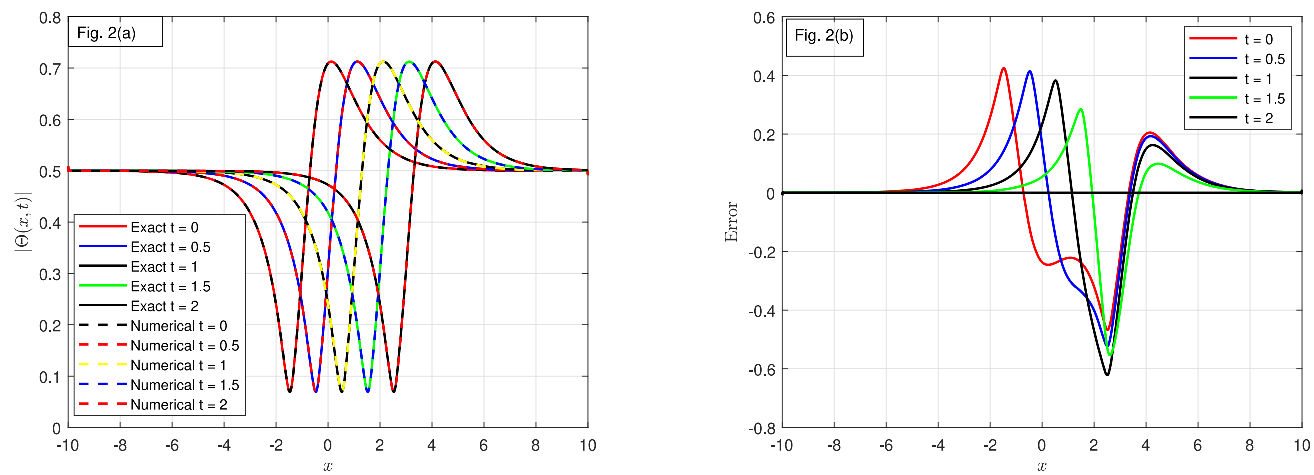

Fig. 2 Figures of Eq. (20) are provided for the constants as follows, $S_1 = 1,\ S_2 = 2,\ \lambda = -1,\ v = 1,\ \varphi = -1,\ \gamma = 1,\ \beta = 1,\ \omega_1 = 1$, and $t = 1.0$ (for $3D$)

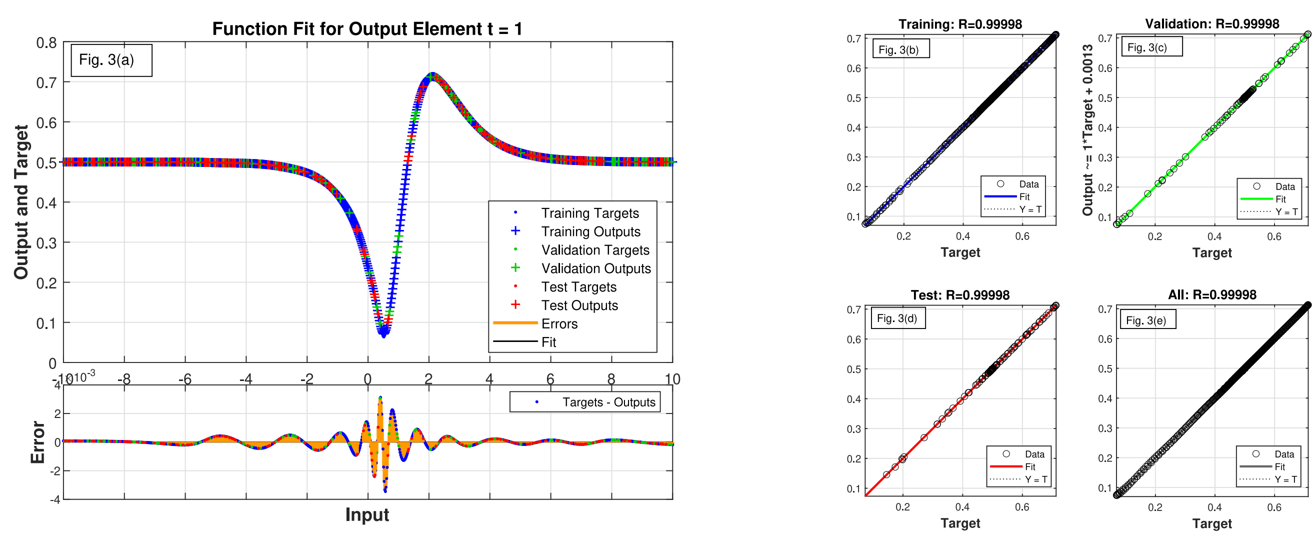

Fig. 3 Figures of Eq. (20) are provided for the constants as follows, $S_1 = 1,\ S_2 = 2,\ \lambda = -1,\ v = 1,\ \varphi = -1,\ \gamma = 1,\ \beta = 1,\ \omega_1 = 1$, and $t = 1$.

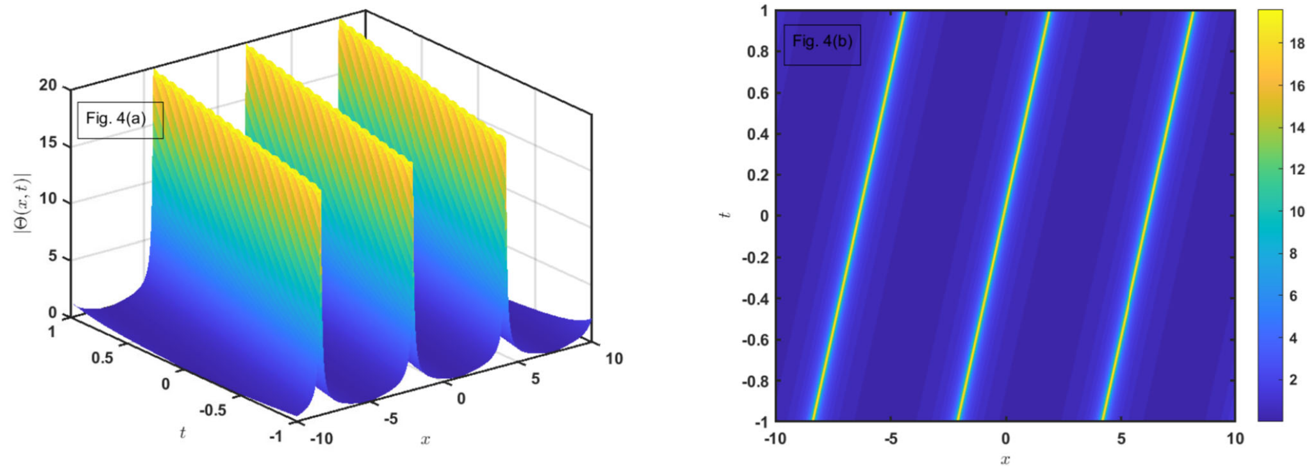

Fig. 4 Figures of Eq. (24) are provided for the constants as follows, $S_1 = 1,\ S_2 = 0.1,\ \lambda = 1,\ v = 0.1,\ \varphi = 0.1,\ \gamma = 1,\ \beta = 1,\ \omega_1 = 1$, and $t = 1$.

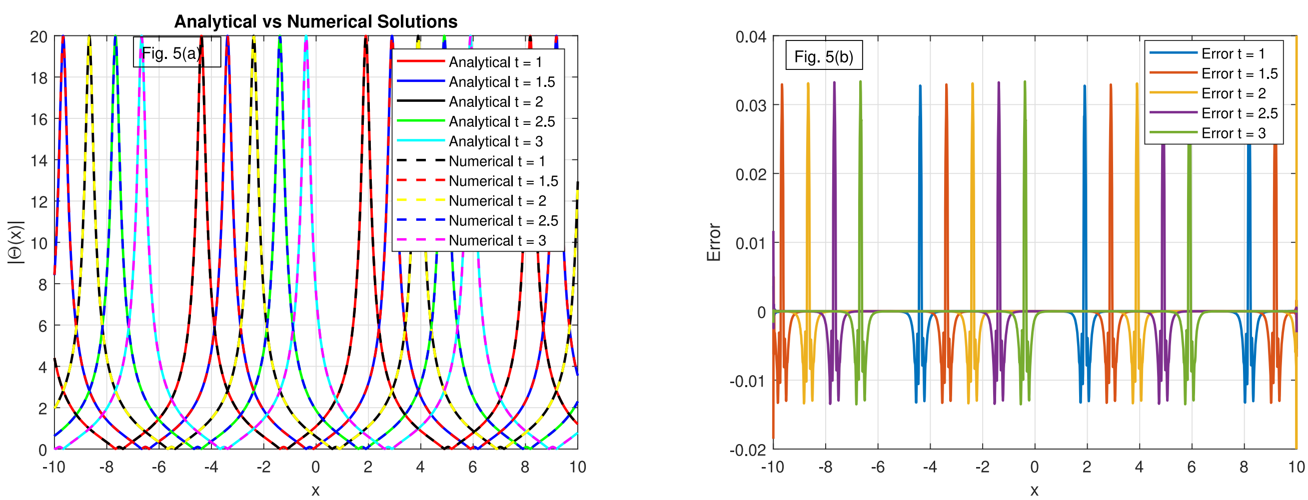

Fig. 5 Figures of Eq. (24) are provided for the constants as follows, $S_1 = 1,\ S_2 = 0.1,\ \lambda = 1,\ v = 0.1,\ \varphi = 0.1,\ \gamma = 1,\ \beta = 1,\ \omega_1 = 1$, and $t = 1$.

artificial neural network training. Figure 1 depicts the oscillatory soliton solution of Eq. (20), with the 3D plot in 1(a) and the contour plot in 1(b) illustrating the exact solution $|\varphi(x,t)|$ over space and time. Figure 1(a) highlights the localized nature of the soliton and its stability as it propagates over time without changing shape. In Fig. 1(b), the color gradient indicates the amplitude intensity, with warmer colors (yellow) representing higher values and cooler colors (black/green) representing lower values. It demonstrates the consistent and localized propagation of the soliton. Figure 3(a) and (b) further demonstrate the effectiveness of the Levenberg-Marquardt artificial neural network in approximating this solution, achieving a remarkably high regression coefficient of $R = 0.99998$ with minimal error (see Fig. 3(c), (d), and 3(e). Figure 2 compares exact and numerical solutions of (14) at different time steps ($t = 0, 0.5, 1.0, 1.5, 2.0$). In Fig. 2(a), soliton peaks for both exact (solid lines) and numerical (dashed lines) solutions are plotted across a range of x-values. The close alignment of these solutions over time highlights the robustness of the numerical approach, although slight variations in amplitude and phase emerge at later time steps. Figure 2(b) presents the error distribution across the x-domain, with dynamic fluctuations in error profiles as time progresses, revealing subtle challenges in maintaining numerical precision. Figures 4, 5, 6 illustrate the periodic soliton solution of (24) with specific parameter values, emphasizing its stable and repeating structure. Figure 4(a) shows the periodic oscillation, while Fig. 5(a) highlights the solitons' stability during propagation. Figure 4(b), the contour plot, provides a detailed view of the intensity variations, with yellow representing peaks and

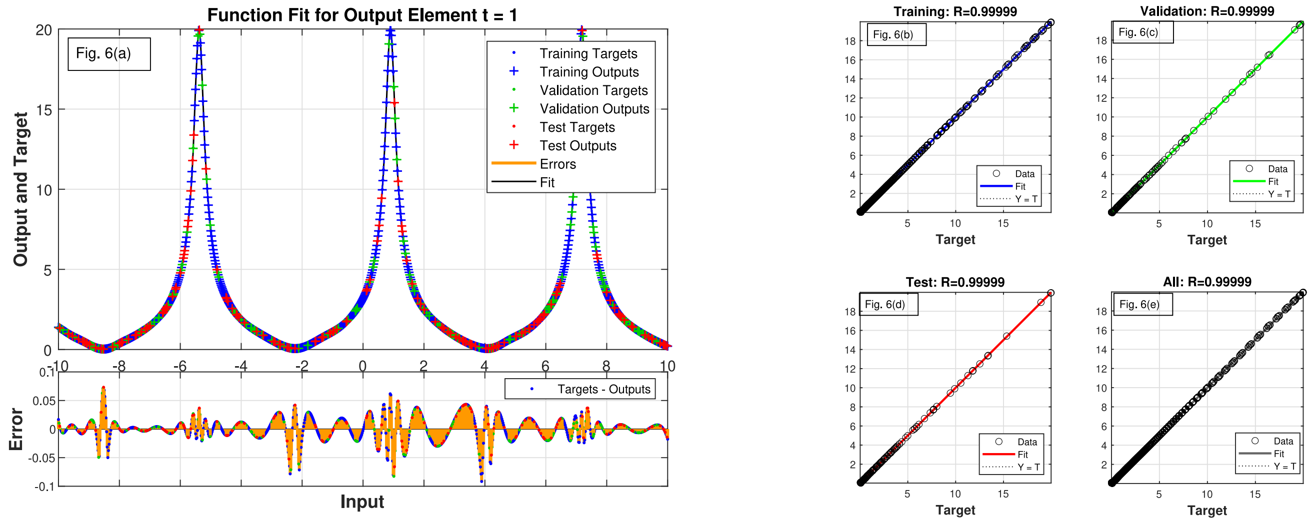

Fig. 6 Figures of Eq. (24) are provided for the constants as follows, $S_1 = 1,\ S_2 = 0.1,\ \lambda = 1,\ v = 0.1,\ \varphi = 0.1,\ \gamma = 1,\ \beta = 1,\ \omega_1 = 1$, and $t = 1$

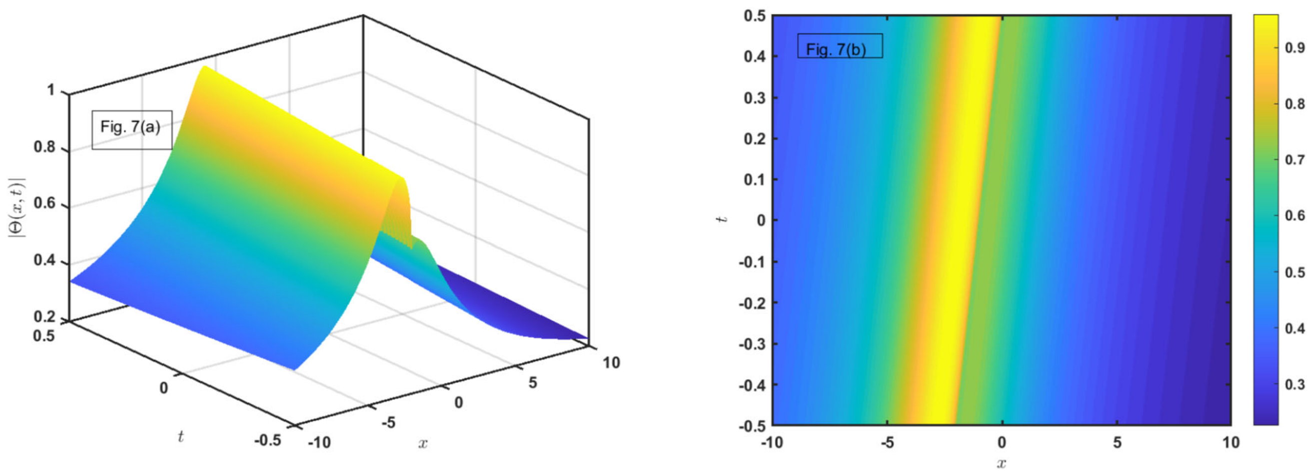

Fig. 7 Figures of Eq. (26) are provided for the constants as follows, $S_1 = 1,\ S_2 = 2,\ \lambda = 1,\ v = 1,\ \varphi = -1,\ \gamma = 1,\ \beta = 1$, and $t = 1$.

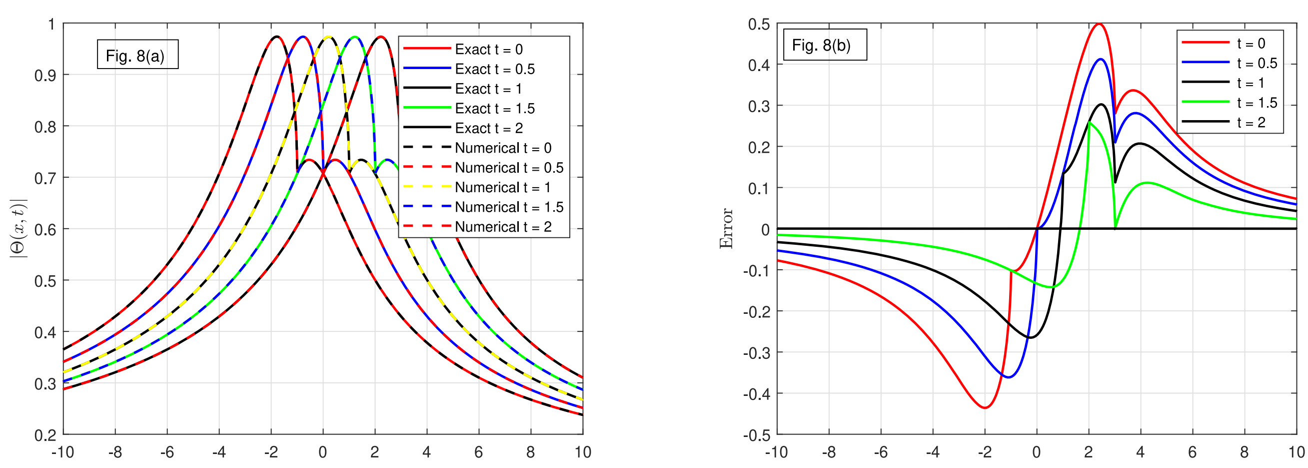

Fig. 8 Figures of Eq. (26) are provided for the constants as follows, $S_1 = 1,\ S_2 = 2,\ \lambda = 1,\ v = 1,\ \varphi = -1,\ \gamma = 1,\ \beta = 1$, and $t = 1$.

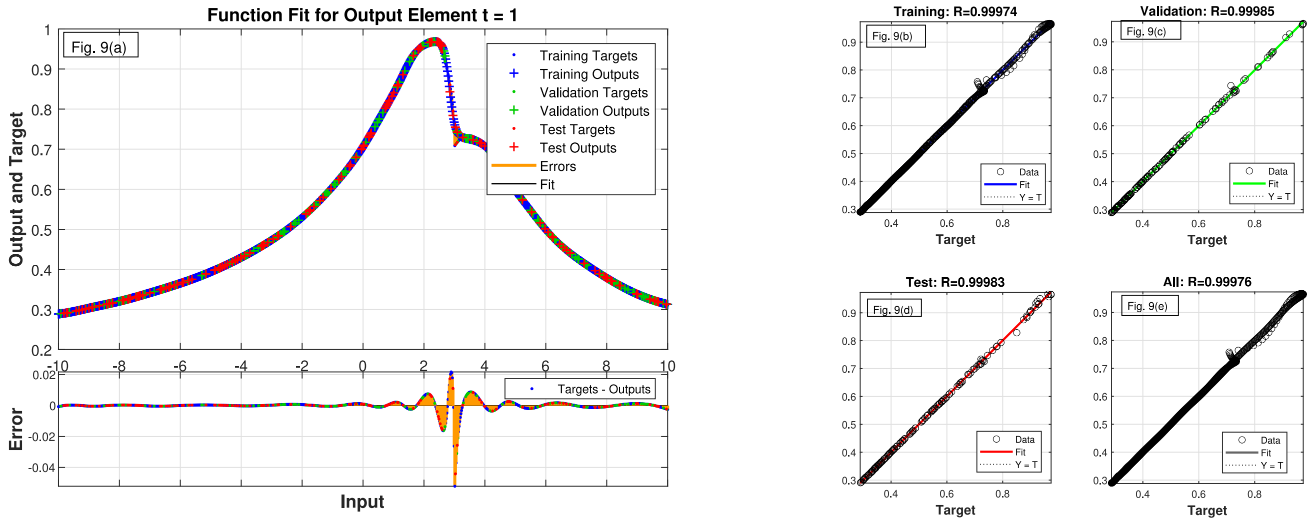

Fig. 9 Figures of Eq. (26) are provided for the constants as follows, $S_1 = 1,\ S_2 = 2,\ \lambda = 1,\ v = 1,\ \varphi = -1,\ \gamma = 1,\ \beta = 1$, and $t = 1$.

black representing troughs. Physically, this reflects stable, periodic localization in nonlinear systems, such as fluid dynamics or plasma oscillations. Figure 5(b) quantifies the error between exact and numerical solutions, showing minor variations indicative of the complexity in simulating dynamic multi-peakon behavior. The precision of the Levenberg-Marquardt artificial neural network in capturing these dynamics is confirmed in Fig. 6, which attains an impressive accuracy of $R = 0.99999$ (see Fig. 6(a), (b), (c), (d), and (e). Finally, Fig. 7 represents the soliton solution for (26), showcasing its dynamic behavior for specific parameter values. In Fig. 7(a), the 3D plot illustrates the gradual evolution of the soliton with localized distribution over x and t. Figure 7(b), the contour plot, highlights the intensity variations, where yellow indicates regions of higher amplitude and black represents lower amplitude regions. Physically, this solution reflects the interaction and stability of wave structures in nonlinear systems, such as fluid flows or plasma oscillations. Figure 8 provides a comparative analysis of exact and numerical solutions for a solitonic wave equation. In Fig. 8(a), soliton profiles are plotted at different time values $t = 0$ to $t = 2$, capturing the evolution of soliton amplitude over space x. Solid lines represent the exact solutions, while the numerical results appear as dashed lines. Figure 8(b) highlights the error between these solutions, with the error increasing in regions of soliton interaction or pronounced oscillations. This panel underscores the accuracy of the numerical method in simulating soliton dynamics over time. The performance of the Levenberg-Marquardt artificial neural network in approximating this solution is further validated in Fig. 9, where regression and fitness graphs demonstrate excellent agreement, with R values ranging from 0.99959 to 0.99999, (see Fig. 9(a), (b), (c), (d), and (e)).

These results collectively affirm the robustness and precision of the Levenberg-Marquardt artificial neural network and split-step Fourier numerical method in approximating a wide range of soliton solutions, further validating the theoretical models presented.

5. Conclusion

In this study, we successfully explored exponential, hyperbolic, trigonometric, and rational function solutions for (14) using the $(\frac{G'}{G}, \frac{1}{G})$-expansion method. By employing three distinct methods–exact solutions, the numerical split-step Fourier method, and the Levenberg-Marquardt artificial neural network we verified the accuracy of our results through detailed graphical analysis and statistical metrics. The combination of tables, graphs, and statistical measures like regression and error curves validated the precision of the numerical and artificial neural network approaches. An essential contribution of this work is integrating the Levenberg-Marquardt artificial neural network, which effectively captured the soliton solutions, providing enhanced accuracy through data-driven techniques. The Levenberg-Marquardt artificial neural network performance, evaluated through fitness plots and statistical comparisons, demonstrated its reliability in approximating complex dynamical behaviors beyond traditional methods. Future research should incorporate advanced physics-informed neural networks to enhance solution accuracy and computational efficiency for nonlinear partial differential equations, making these methods more applicable to real-world complex systems.

Acknowledgements Aamir Farooq acknowledges the postdoctoral fellowship supported by Zhejiang Normal University, China, under Grant No. YS304024913. Wen Xiu Ma acknowledges support from the Ministry of Science and Technology of China (G2021016032L and G2023016011L), the National Natural Science Foundation of China (NSFC) under grants 12271488 and 11975145.

Author contributions Aamir Farooq: Conceived and designed the analysis; Analyzed and interpreted the data; Wrote the paper. J. R. M. Borhan: Analyzed and interpreted the data; Contributed analysis tools or data; Wrote the paper. Sadique Rehman: Analyzed and interpreted the data; Contributed analysis tools or data; Wrote the paper. M. Mamun Miah: Analyzed and interpreted the data; Wrote the paper. Wen Xiu Ma: Review the paper; and Supervision.

Data availability The data supporting this study's findings are available in the article.

Declarations

Conflict of interest The authors declare that they have no Conflict of interest.

References

[1] L Debnath *Nonlinear Partial Differ.Eq. Sci. Eng.* Springer (2005).
[2] M Wang, X Li and J Zhang *Phys. Lett. A* **372** 417 (2008).
[3] A Aasaraai *British J. Math. Comput. Sci.* **11** 1 (2015).
[4] A Kumar and R D Pankaj *J. Egyptian Math.Soc.* **23** 282 (2015).
[5] S Yuzbasi *Appli. Math. Modell.* **40** 5349 (2016).
[6] A Biswas, M Mirzazadeh, M Eslami, Q Zhou, A Bhrawy and M Belic *Optik* **127** 7250 (2016).
[7] K R Raslan and M A Abd El salam K K Ali E M Mohamed *J. Egyptian Math. Soc.* **27** 1 (2019).
[8] W X Ma *Partial Differ. Equ. Appl. Math.* **5** 100220 (2022).
[9] I P Jordanov *AIP Conference Proceedings* 2459 (2022).
[10] G Akram, M Sadaf and M A U Khan *Optik* **252** 168372 (2022).
[11] O Bazighifan, H Ahmad and S W Yao *Mathematics* **8** 728 (2020).
[12] K K Ali, R Yilmazer, H M Baskonus and H Bulut *Physica Scripta* **95** 065602 (2020).
[13] R Amin N Patanarapeelert M A Barkat I Mahariq T Sitthiwirattham *J. Funct. Spaces* (2022).
[14] A Hussain, A H Kara and F D Zaman *Chaos Solitons & Fractals* **171** 113423 (2023).
[15] T Rasool, R Hussain and M A Al Sharif W Mahmoud M S Osman *Opt. Quantum Electron.* **55** 396 (2023).
[16] J R M Borhan, A H Ganie, M M Miah, M A Iqbal, A R Seadawy and N K Mishra *Opt. Quantum Electron.* **56** 938 (2024).
[17] S Soradi-Zeid and M Alipour *J. Computati. Appl. Math.* **436** 115410 (2024).
[18] N Raza, B Rani, Y Chahlaoui and N A Shah *Nonlinear Dyn.* **111** 18419 (2023).
[19] R Mia M M Miah M S Osman *Available at SSRN 4367585* (2023).
[20] H Zhang, Y X Chen, L Wei, F P Wang, W P Zhang and W S Duan *J. Plasma Phys.* **89** 905890212 (2023).
[21] M A Shihab, W M Taha, R A Hameed, A Jameel and I M Sulaiman *Int. J. Electric. Comput. Eng.* **13** 2131 (2023).
[22] H Yasmin, A S Alshehry, A H Ganie, A Shafee and R Shah *Sci. Rep.* **14** 1810 (2024).
[23] M Senol, L Akinyemi, H Nkansah and W Adel *J. Ocean Eng. Sci.* **9** 59 (2024).
[24] A H Arnous, M S Hashemi, K S Nisar, M Shakeel, J Ahmad, I Ahmad, R Jan, A Ali, M Kapoor and N A Shah *Results Phys.* **57** 107369 (2024).
[25] M Shakeel Attaullah N A Shah J D Chung *Symmetry* **15** 360 (2023).
[26] A Mumtaz, M Shakeel, A Manan, M Kouki and N A Shah *AIMS Mathematics* **10** 9516 (2025).
[27] L X Li, E Q Li and M L Wang *Appl. Math. -A J. Chin. Univ.* **25** 454 (2010).
[28] M N Hossain, M M Miah, F Z Duraihem and S Rehman *Opt. Quantum Electron.* **56** 1 (2024).
[29] Z Sabir, M A Z Raja, J L G Guirao and T Saeed *Chaos Solitons & Fractals* **152** 111404 (2021).
[30] Y Fang, G Z Wu, N A Kudryashov, Y Y Wang and C Q Dai *Chaos Solitons & Fractals* **158** 112118 (2022).
[31] M Raissi, P Perdikaris and G E Karniadakis *J. Computat. Phys.* **378** 686 (2019).
[32] L Wang and Z Yan *Phys. Lett. A* **404** 127408 (2021).
[33] E Kharazmi, Z Zhang and G E Karniadakis *Comput. Methods Appl. Mech. Eng.* **374** 113547 (2021).
[34] X Jin, S Cai, H Li and G E Karniadakis *J. Computat.Phys.* **426** 109951 (2021).
[35] T N Cheema, M A Z Raja, I Ahmad, S Naz, H Ilyas and M Shoaib *Europ. Phys. J.Plus* **135** 1 (2020).
[36] A Waheed, M Awais, M A Z Raja, M Y Malik and A S Alqahtani *Int. Commun. Heat Mass Transfer* **152** 107321 (2024).
[37] R Hirota *The Direct Method in Soliton Theory* Cambridge University Press (2004).
[38] M J Ablowitz H Segur *Solitons and the Inverse Scattering Transform* SIAM (1981).
[39] O V Sinkin, R Holzlöhner, J Zweck and C R Menyuk *J. Lightwave Technol.* **21** 61 (2003).
[40] S Sapna, A Tamilarasi and M P Kumar *Comp. Sci. Inform. Technol. (CS and IT)* **2** 393 (2012).
[41] E M E Zayed, A G Al-Nowehy and R M A Shohib *J. Ocean Eng. Sci.* **4** 14 (2019).
[42] J Pedlosky *J. Atmos. Sci.* **27** 15 (1970).
[43] M Pawlik and G Rowlands *J Phys. C Solid State Phys.* **8** 1189 (1975).
[44] D Lu A R Seadawy M Arshad *Opt. Quantum Electron.* **50** 1 (2018).
[45] Y Pandir and A Ekin *Chin. J. Phys.* **67** 534 (2020).